HHS Public Access

Author manuscript

Phys Med Biol. Author manuscript; available in PMC 2023 July 05.

Published in final edited form as:

Phys Med Biol. ; 67(17): . doi:10.1088/1361-6560/ac88b5.

Interstitial fluid streaming in deep tissue induced by ultrasound momentum transfer for accelerating nanoagent transport and controlling its distribution

Baohong Yuan[1,2]

[1]Ultrasound and Optical Imaging Laboratory, Department of Bioengineering, The University of Texas at Arlington, Arlington, TX 76019, USA

[2]Joint Biomedical Engineering Program, The University of Texas at Arlington and The University of Texas Southwestern Medical Center at Dallas, Dallas, TX 75390, USA

Abstract

Objective: This study aims to theoretically investigate the dynamics of ultrasound-induced interstitial fluid streaming and tissue recovery after ultrasound exposure for potentially accelerating nanoagent transport and controlling its distribution in tissue.

Approach: Starting from fundamental equations, the dynamics of ultrasound-induced interstitial fluid streaming and tissue relaxation after an ultrasound exposure were modeled, derived and simulated. Also, both ultrasound-induced mechanical and thermal effects were considered in the models.

Main Results: The proposed new mechanism was named squeezing interstitial fluid via transfer of ultrasound momentum (SIF-TUM). It means that an ultrasound beam can squeeze the tissue in a small focal volume from all the directions, and generate a macroscopic streaming of interstitial fluid and a compression of tissue solid matrix. After the ultrasound is turned off, the solid matrix will recover and can generate a backflow. Rather than the ultrasound pressure itself or intensity, the streaming velocity is determined by the dot product of the ultrasound pressure gradient and its conjugate. Tissue and nanoagent properties also affect the streaming and recovery velocities.

Significance: The mobility of therapeutic or diagnostic agents, such as drugs, drug carriers, or imaging contrast agents, in the interstitial space of many diseased tissues, such as tumors, is usually extremely low because of the inefficiency of the natural transport mechanisms. Therefore, the interstitial space is one of the major barriers hindering agent deliveries. The ability to externally accelerate agent transport and control its distribution is highly desirable. Potentially, SIF-TUM can be a powerful technology to accelerate agent transport in deep tissue and control the distribution if appropriate parameters are selected.

Keywords

Drug delivery; Nanoagent delivery; Ultrasound; Streaming; Fluorescence; Modeling; Simulation

Correspondence author: Baohong Yuan, Ph.D., FSPIE, Distinguished University Professor, Marsha and Bill Carroll Endowed Faculty Fellow, Professor of Bioengineering, University of Texas at Arlington, 500 UTA BLVD, Arlington, TX 76010, Tel: 817-272-2917 (Office), baohong@uta.edu.

1. Introduction:

Currently, the transport and distribution of therapeutic or diagnostic agents (such as drugs, drug carriers, or imaging contrast agents) in a tumor or other tissues are uncontrollable (Shi et al., 2017; McNamara and Tofail, 2017; Barua and Mitragotri, 2014; Soares et al., 2018). Extremely low mobility in tissue interstitial space is one of the major barriers to agent delivery. Two natural transport mechanisms in interstitial space are (1) diffusion due to concentration gradient and (2) convection via natural interstitial fluid flow. Both depend on natural and random motions. Diffusion is a slow procedure, especially for the large-sized agents (>10 nm). Convection is usually disrupted due to pathologic conditions, such as elevated interstitial fluid pressure (IFP) in tumors (Leunig et al., 1992; Netti et al., 1995). This may lead to a heterogeneous distribution and failures of treatment or diagnosis. Therefore, the ability to externally accelerate agent transport and control its distribution is highly desirable.

Using ultrasound to enhance drug delivery efficiency has been investigated during the past years. Usually, it is believed that ultrasound can generate mechanical and thermal effects to increase tissue permeability and further the diffusivity of agents (Ranjan et al., 2012; Yuh et al., 2005; O'Neill et al., 2009; Ziadloo et al., 2013; Lee et al., 2013; Pitt, 2008; Frenkel, 2008; Tebebi et al., 2017; Hancock et al., 2009; de Smet et al., 2011; Deckers and Moonen, 2010; Park et al., 2013; Dromi et al., 2007; Grüll and Langereis, 2012; Sarvazyan et al., 2010, Yeh and Juárez, 2021). On the other hand, the feasibility and efficiency of using ultrasound to induce interstitial fluid streaming to enhance delivery via a convection-based method are much less investigated. Also, contradictory results are reported in the literature. For example, ultrasound-induced streaming of fluid stained with a dye has been observed via a microscope at the boundary between a porous material and a water bath (El Ghamrawy et al., 2019). The authors observed that the dye molecules were pushed along both axial and lateral directions by using a 5-MHz ultrasound beam (focal length: 35 mm, diameter: 33mm) with 238 W/cm^2 spatial peak time average intensity. Eckart's acoustic streaming velocity equation (Eckart, 1948) was modified to explain the experimental results. The major limitations of this study include the following. (1) Fluid streaming occurring at the boundary between a tissue-mimic solid phantom and a fluid (such as a water bath) is not practically relevant to the application of enhancing agent delivery. This is because streaming at a boundary may be much easier to achieve and observe than when the ultrasound focus is completely in tissue or a phantom. (2) The adopted Eckart's equation is based on acoustic radiation force (ARF), which only has one component acting in the axial direction while the lateral forces are assumed to be zero. (3) The model only considers the fluid motion and does not include the interaction between solid and fluid material. This may be suitable for the situations when streaming occurs in a fluid or at the solid-and-fluid boundary, but may be questionable for the situation inside tissue. (4) The model is a static model and does not show the streaming dynamics and what happens after an ultrasound exposure.

When using an ultrasound to push nanoparticles into a tissue-mimic phantom, a recent study shows a contradictory result (Løvmo et al., 2021). In this study, a collagen gel was adopted to mimic tumor extracellular matrix (ECM). Ultrasound-induced motion of PEGylated

poly(2-ethyl-butyl cyanoacrylate) nanoparticles with a diameter between 140 and 195 nm and loaded with a fluorescence dye NR668 was investigated via confocal laser scanning microscopy. The adopted ultrasound transducer has a frequency of 10 MHz (focal length: 50 mm, diameter: 19 mm). ARF-induced gel deformation was found, but no AFR-induced nanoparticle penetration enhancement was observed in the adopted gel phantom. Authors attributed this negative result to the low acoustic absorption of the adopted phantom, which results in a small ARF, and a low ultrasound pressure and duty cycle. Authors used the Darcy's law combined with an ARF-based model to analyze possible fluid streaming distance in the phantom. Based on this model and the adopted experimental conditions, authors claimed that the maximum ARF-induced streaming distance is ignorable compared with the AFR-induced tissue deformation.

Successful models can guide researchers to select appropriate tissues (or phantoms) and experimental conditions to investigate this phenomenon. The major limitations of the conventional ARF-based theories include that tissue is considered a single-phase and incompressible material, and the ARF density (i.e., force per unit volume) is directly used for calculating the pressure gradient in the Darcy's law (Løvmo et al., 2021). When tissue is considered a single-phase and incompressible material, the concept of ARF is suitable for understanding the ultrasound-induced tissue distortion (or displacement). However, most biological soft tissues are bi-phase materials including both fluid and solid matrix, and usually considered viscoelastic porous materials. The relative motion between the fluid and the solid is possible under appropriate conditions (i.e., compressible materials). Therefore, the models to describe streaming in tissue are different from those in a pure fluid or gas. Thus, it is necessary to understand and model the phenomenon of ultrasound-induced interstitial fluid streaming in tissue from the fundamental equations.

Because tissue fluid is the primary component in the streaming phenomenon, the concept of the hydrostatic pressure of the interstitial fluid is more suitable for understanding the mechanism than the ARF. Ultrasound-induced hydrostatic pressure change of interstitial fluid has been used to investigate streaming in tissue (Raghavan, 2018). However, the related models in the literature are limited and have not provided a clear and full picture about the dynamics of the streaming and relaxation in tissue. Based on the idea using the hydrostatic pressure (Raghavan, 2018) and combining with the acoustic perturbation method (Prieur and Sapozhnikov, 2017) and a bi-phase model (Zhang et al., 2008; Kwan et al., 1984; Ehlers and Markert, 2001), this study aims to provide a full picture to understand the dynamics of ultrasound-induced interstitial fluid streaming in tissue and its relaxation. Meanwhile, the models used in this study will also include both ultrasound-induced mechanical and thermal effects. Thus, their effects can be compared and optimized for experiment guidance.

Another motivation is because of an interesting phenomenon that we observed in our ultrasound-switchable fluorescence (USF) imaging of tumors. USF is a high-resolution deep-tissue hybrid imaging technology, which uses a focused ultrasound beam to control fluorescence emission in tissue (Yao et al., 2019; Pei et al., 2014; Cheng et al., 2016; Yuan et al., 2012; Yu et al., 2020b; Liu et al., 2020b; Yao et al., 2021; Yu et al., 2020a). Recently, during USF imaging experiments, the following phenomenon was discovered. First, USF nanoagents, poly (N-isopropylacrylamide) nanoparticles with a diameter of ~32

nm encapsulated with β-cyclodextrin and indocyanine green complexes (Liu et al., 2020a), were intravenously injected into a mouse with a tumor. About 6 hours after the injection, these nanoagents were accumulated in the tumor. Then, USF imaging was conducted. Our images showed that a portion of these nanoparticles could be pushed away from the ultrasound focal volume (a 2.5-MHz ultrasound beam with a lateral and axial focal size of ~0.5 and ~3.5 mm, respectively). To understand this phenomenon, SIF-TUM mechanism was proposed in this study. While the detailed experimental studies can be published in future, for readers to better understand SIF-TUM, Fig. 1 shows a commonly used setup in USF imaging. A focused ultrasound transducer (FUST) was used to deliver an ultrasound wave into a tumor (T). Two optical fiber bundles (LF) were used to deliver excitation light to illuminate the tumor, and a camera (EMCCD) was used to detect the fluorescence emission from the USF contrast agents. The models provided in this study show that SIF-TUM is different from the conventional ultrasound enhancement methods that aim to increase tissue permeability and diffusivity. Instead, SIF-TUM squeezes the tissue in a small ultrasound focal volume from all directions to generate a macroscopic streaming of interstitial fluid from a millimeter-sized focus. When ultrasound is off, a backflow occurs due to the elastic property of tissue solid matrix, which generates an expansion. Thus, a tissue compression-and-expansion motion occurs, which is different from the ARF-induced tissue translational displacement.

2. Models and Simulations:

2.1 Background of theories and a general description about SIF-TUM

The conventional theories, such as ARF (Aglyamov et al., 2007; Sarvazyan et al., 1998; Doherty et al., 2013; Bruus, 2012a, 2011, 2012b; Wu, 2018; Eckart, 1948; Lighthill, 1978) or pulsed ultrasound-induced mechanical and thermal effects (Ranjan et al., 2012; Yuh et al., 2005; O'Neill et al., 2009; Ziadloo et al., 2013; Lee et al., 2013; Pitt, 2008; Frenkel, 2008; Tebebi et al., 2017; Hancock et al., 2009; de Smet et al., 2011; Deckers and Moonen, 2010; Park et al., 2013; Dromi et al., 2007; Grüll and Langereis, 2012; Sarvazyan et al., 2010), have been well studied and widely used to quantify ARF-induced tissue displacement, shear waves for measuring tissue stiffness, and ultrasound-induced tissue thermal effects. Unfortunately, these theories failed to predict the SIF-TUM phenomenon because they consider tissue a single-phase material (and another possible reason can be found in the supplementary materials). As mentioned before, the relative motion between the fluid and the solid matrix is possible when tissue interacts with an externally applied force or radiation (Zhang et al., 2008; Kwan et al., 1984; Ehlers and Markert, 2001). One scenario that can help to understand this motion is that a groove can be observed on the skin after being pressed by a sharp object or long-term use of a rubber band. The mechanism is that the tissue fluid is pushed away from the applied area, and the solid matrix of tissue is deformed under the pressure. After completing the pressing, the skin will gradually recover (i.e., the disappearing of the groove), which takes much longer time than the pressing time.

Similarly, one can imagine that SIF-TUM squeezes the tissue in a small ultrasound focal volume from all directions (~0.7 mm^3 in this work). The interstitial fluid can move relative to the solid matrix depending upon the hydrostatic pressure gradient. When the fluid moves

away from the original location, the space should be occupied by the solid matrix if no void space exists (i.e., no cavitation), which indicates the solid matrix is deformed. Therefore, SIF-TUM-induced fluid motion and solid matrix deformation should be differentiated from ARF-induced tissue displacement. The former is a type of compression-and-expansion motion, whereas the ARF-induced tissue displacement can be considered a translational motion typically along a primary direction that is usually the force direction. In practice, these two motions may be superposed. One can imagine these two phenomena as follows. When an ultrasound beam is focused in tissue, in the focal volume the ARF will push the tissue forward along the wave axial direction (Z) and generate a small tissue displacement. Meanwhile, the ultrasound wave will also pass a portion of its momentum to the fluid, which will lead to a "splash" of the fluid moving out of the focal volume and thus the deformation of the solid matrix. Because the tissue hydraulic conductivity is usually small, it can function as a resistance to the motion of the fluid. Thus, the "splashed" fluid will be accumulated somewhere around the area, and it further leads to the elevation of the hydrostatic pressure in the focal volume. Mathematically, the spatial nonuniform momentum transfer at different locations in the focal volume will induce a nonuniform increase of fluid hydrostatic pressure (see Equation 1 in Table 1). Based on Darcy's law, the gradient of this hydrostatic pressure will drive the motion of the fluid, which is called an exudation flow, and will create a type of macroscopic streaming at a size slightly larger than the ultrasound focal size. After the ultrasound is off, the fluid can backflow into the original volume because the source of the hydrostatic pressure is lost, and the solid matrix will recover due to its elasticity. However, the speed of this recovery depends on the tissue properties and how significant the solid tissue is compressed, which may take a much longer time than the time to generate this deformation (the details will be discussed).

In summary, there are three types of motions that should be differentiated clearly. First, the ultrasound pressure wave can induce tissue local oscillations at the ultrasound frequency and its harmonic frequencies (usually at the MHz level). When investigating this type of motion, tissue is considered a single-phase mixture of fluid and solid. It is not necessary to differentiate the fluid from the solid because the frequency is so high that both fluid and solid will oscillate at the same velocity. Second, the ultrasound pressure wave can also induce much slower motions compared with the MHz oscillations, such as the ARF-induced tissue displacement (a translational motion) or a shear wave motion induced by a pulsed or oscillated ARF (a low-frequency oscillation) (Sarvazyan et al., 1998). In this type of motion, tissue is also considered a single-phase mixture of fluid and solid because both components move at the same velocity under a net ARF. Third, the ultrasound pressure can also induce a compression-and-expansion (or squeezing-and-recovering) motion at a much lower speed than the speed of the MHz oscillation, which generates a relative motion between tissue fluid and solid matrix (i.e., the SIF-TUM phenomenon). In this type of motion, the speed of the tissue fluid motion should be differentiated from that of the solid matrix. Assuming no void space can be generated, the exudation fluid velocity from the focal volume (W_2) will be assumed to be equal to the negative velocity of the solid matrix (V_s), which means $W_2 = -V_s$ (Raghavan, 2018).

2.2 Equations of the models

All the equations have been summarized in Table 1, and the related variables, operators, their physical meanings, and the adopted values (from the literature for soft tissues or tumors) in the simulations have been listed in Table 2. Each equation is explained in the following paragraphs. Due to the lengthy derivation procedures, the final equations are directly provided in this paper. The adopted mathematic methods may be found in the references provided in each paragraph.

(1) Equation 1—Ultrasound induces interstitial fluid hydrostatic pressure increase (P_{hs}) via ultrasound momentum transfer: Briefly, the ultrasound pressure wave $P(r,t)$, ultrasound-induced tissue density $\rho(r,t)$, and tissue oscillation velocity $V(r,t)$ can be expressed as Equations 0a-0c in Table 1 (Wu, 2018; Raghavan, 2018; Bruus, 2012a, 2011; Prieur and Sapozhnikov, 2017; Lighthill, 1978; Eckart, 1948). In Equations 0a-0c, r and t represent the location and time; the subscripts of 0, 1, and 2 indicate the 0th, 1st, and 2nd order of the quantities, respectively; $\omega = 2\pi f$ is the ultrasound angular frequency, and $f = 2.5$ MHz in this study; $c.c.$ is complex conjugates. This representation is commonly used in the literature to separate the time and space variables for sinusoidal oscillations. For convenience, all the symbols of r in the parentheses on the right hand side of the three equations will be ignored in the following sections (but readers should be aware that they are functions of r but are independent of time). Any quantities or their multiplications with an order higher than 2nd were ignored.

Thus, inserting these variables into the mass conservation (i.e., continuity equation) and Navier–Stokes equation (eventually reduced to Darcy's law equation) (Raghavan, 2018; Prieur and Sapozhnikov, 2017; Bruus, 2012a), the first key equation was derived: $\nabla^2 P_{hs} \approx \frac{(\phi_f/\phi_s)}{\rho_0 K} \nabla \bullet \langle \rho_1 V_1 \rangle \approx -\frac{\alpha(\phi_f/\phi_s)}{c_0 K \omega^2 \rho_0^2} \left[\nabla P_1 \bullet \nabla P_1^* \right]$ (i.e., Equation 1 in Table 1). P_{hs} is a 2nd-order small quantity and represents the ultrasound-induced increase of local hydrostatic pressure of the interstitial fluid at a specific location in the tissue.

This equation is the most important result and the foundation of the SIF-TUM phenomenon. It indicates that P_{hs} is generated by the divergence of the temporal average of the 1st-order momentum density of the ultrasound wave (i.e., $\nabla \bullet \langle \rho_1 V_1 \rangle$). Here, $\rho_1 V_1$ is the 1st-order momentum density of the ultrasound wave at a specific location and time. $\langle \square \rangle$ represents the temporal average in one ultrasound oscillation cycle. Physically, because the ultrasound wave loses momentum and transfers it to tissue, $\nabla \bullet \langle \rho_1 V_1 \rangle$ should be a negative value. This momentum transfer from ultrasound to tissue fluid leads to a local hydrostatic pressure rise (P_{hs}) of the tissue fluid because of a finite value of the hydraulic conductivity of tissue (K). If K was an infinite large value, P_{hs} would be zero because K is in the denominator. It is worth pointing out that the contributions from other mechanisms (Raghavan, 2018) have been ignored during the derivation because their contributions are minor compared with that from the term of $\nabla \bullet \langle \rho_1 V_1 \rangle$.

Further, the term of $\frac{(\phi_f/\phi_s)}{\rho_0 K}\nabla \bullet \langle \rho_1 V_1 \rangle$ can be expressed as $-\frac{\alpha(\phi_f/\phi_s)}{c_0 K \omega^2 \rho_0^2}\left[\nabla P_1 \bullet \nabla P_1^*\right]$ (see the Equation 1), which is derived by using the similar method to that used in the reference (Prieur and Sapozhnikov, 2017) and has not been reported in the literature. It involves the tissue ultrasound absorption coefficient (α), the volume fraction ratio of the tissue interstitial fluid and solid matrix (ϕ_f/ϕ_s), the sound speed (c_0), the hydraulic conductivity of tissue (K), the square of tissue's 0th order density (ρ_0^2), the square of the ultrasound angular frequency (ω^2), and ∇P_1 (the gradient of the 1st order complex amplitude of the ultrasound pressure P_1). Note that ∇P_1 is a vector. ∇P_1^* is the complex conjugate of ∇P_1 and is also a vector. The symbol of $\bullet$ is the dot product between the two vectors. This result clearly shows that P_{hs} is determined by $\left[\nabla P_1 \bullet \nabla P_1^*\right]$ rather than the pressure itself or the square of pressure (which is frequently seen in the literature when the ARF-based model is used (Løvmo et al., 2021, (El Ghamrawy et al., 2019))). Note that $\left[\nabla P_1 \bullet \nabla P_1^*\right]$ can be further represented as $\left[\left(\frac{\partial R}{\partial x}\right)^2+\left(\frac{\partial I}{\partial x}\right)^2\right]+\left[\left(\frac{\partial R}{\partial y}\right)^2+\left(\frac{\partial I}{\partial y}\right)^2\right]+\left[\left(\frac{\partial R}{\partial z}\right)^2+\left(\frac{\partial I}{\partial z}\right)^2\right]$, where R and I are the real and imaginary parts of P_1, respectively. Because each term is squared, $\left[\nabla P_1 \bullet \nabla P_1^*\right]$ is positive. Therefore, the negative sign in front of the right-hand part of Equation 1 further indicates that $\nabla \bullet \langle \rho_1 V_1 \rangle$ is negative.

(2) Equation 2(a) —The gradient of elevated hydrostatic pressure (∇P_{hs}) induces the exudation fluid velocity (W_2): Once P_{hs} is calculated from Equation 1, based on Darcy's law (Raghavan, 2018) the exuding velocity of the fluid from the focal volume can be calculated using the following equation: $W_2 = -K\nabla P_{hs} = -V_s$, where K is the tissue's hydraulic conductivity and can be expressed as the ratio of tissue permeability (k) to fluid viscosity (μ). Once W_2 is calculated, the velocity of the solid matrix (V_s) is known. The squeezing-caused displacement (i.e., compression) u_s can be integrated from t = 0 to t_0 (ultrasound exposure time) using the equation of $u_s = \int_0^{t_0} V_s dt$ as shown in Equation 2a. Equation 2a shows that the elevation of the hydrostatic pressure (P_{hs}) in ultrasound focal volume will lead to the exudation of the fluid from the focal volume with an outward velocity of W_2 (a positive value), and therefore, it will lead to the compression of the tissue solid matrix with an inward velocity V_s (a negative value). Depending on the value of $\left[\nabla P_1 \bullet \nabla P_1^*\right]$, a typical value of this flow velocity can reach a level of microns/second, which is much higher than the typical value of the natural flow velocity in a tumor (<1 micron/second) (Baxter and Jain, 1989). The velocity of this flow is controllable via $\left[\nabla P_1 \bullet \nabla P_1^*\right]$, which functions as a convection transport mechanism and brings the nanoagents out of the focal volume. One can imagine it as a pumping procedure when the ultrasound is turned on. This is much more efficient and controllable than altering tissue permeability and diffusivity as per the conventional methods.

Equation 2(b) —Turning off ultrasound leads to a backflow of the fluid (W_2) because of the recovery of the solid matrix: When ultrasound is turned off, the driving force is removed (i.e., $\left[\nabla P_1 \bullet \nabla P_1^*\right] = 0$), and P_{hs} decays to zero almost immediately (due to the extremely fast decay speed of the hydrostatic pressure relaxation). The compressed solid matrix tends to expand and recover to its original position at a velocity

of V_s due to its elasticity (described by an apparent modulus H) (Zhang et al., 2008; Kwan et al., 1984). This expansion will suck the fluid back into the focal volume because any expanded volume must be filled by fluid (assuming no void space occurs in tissue). The velocity of tissue solid matrix can be described via a bi-phase model (Zhang et al., 2008; Kwan et al., 1984; Ehlers and Markert, 2001), which can be expressed as $KH\nabla^2 u_s = \frac{\partial u_s}{\partial t} = V_s$ and listed as Equation 2b in Table 1. u_s is the displacement of the solid matrix from its original position, and V_s is its velocity. Note that the initial spatial distribution of u_s can be calculated from the previous step in Equation 2a. Once u_s is calculated, V_s can be calculated based on $V_s = \frac{\partial u_s}{\partial t}$. The recovery velocity of V_s at the early stage is usually high because of the large deformation of the solid tissue (i.e., high value of $\nabla^2 u_s$, which reduces with the solid tissue recovery) and tissue's high apparent modulus (H) (Zhang et al., 2008; Kwan et al., 1984; Ehlers and Markert, 2001). Once V_s is calculated, W_2 is known based on $W_2 = -V_s$ in Equation 2b. Our simulation results showed that a portion of the fluid can quickly flow back into the original focal volume, but the rest of fluid will flow back slowly. This is important and favorable for controlling agent distribution. First, quickly recovering tissue fluid will allow repeating this procedure without mechanically damaging tissue due to the significant loss of tissue fluid in the focal volume. Second, the slow backflow avoids a complete recovery of the agents, and therefore, it allows continuously pumping the agents out of the focal volume at a future time via an accumulation effect.

(3) Equation 3—Ultrasound induces a tissue temperature rise (Δ*T*) due to tissue absorption of acoustic energy and Δ*T* decays when ultrasound is off: For safety reasons, it may be necessary to limit the maximum temperature increase ΔT to a preset value of ΔT_0, which is eventually regulated by a thermal index. Also, the gradient of ΔT can affect agent distribution via thermophoresis (Wongsuwarn et al., 2012). It is necessary to calculate ΔT using a bio-heat transfer equation (Vyas and Rustgi, 1992; Anand and Kaczkowski, 2008), which is Equation 3a in Table 1. When ultrasound is off, the decay of ΔT is described via Equation 3b by simply setting the amplitude of P_1 as zero (i.e., $|P_1| = 0$). In Equation 3, c_t and c_b are the specific heat capacity of tissue and blood, respectively. k_t is the tissue thermal conductivity. ρ_0 and ρ_b are the density of tissue and blood, respectively. ω_b is the blood perfusion rate. c_0 is the speed of sound in tissue.

(4) Equation 4—Ultrasound induces agent concentration change due to three different mechanisms: After W_2 and ΔT are calculated from Equations 2 and 3, the dynamic change of agent concentration can be calculated based on the continuity equation (i.e., Equation 4 in Table 1). C is the agent concentration. J is the total flux due to agent transport via three mechanisms, including diffusion due to concentration gradient ($-D_{BD}\nabla C$) (Ramanujan et al., 2002), thermophoresis due to ultrasound-induced temperature gradient ($-CD_{TP}\nabla(T)$) (Duhr and Braun, 2006), and the SIF-TUM induced flow of interstitial fluid ($CR_f W_2$). σ_s and σ_i are the rate of source and sink of the agents. In this study, for simplicity, we assume $\sigma_s = \sigma_i = 0$. This means no extra sources and sinks can create or destroy, respectively, the agents during the investigation time period. D_{BD} and D_{TP} are the agent diffusion coefficient and thermophoresis diffusion coefficient, respectively. The

agent diffusion coefficient D_{BD} is calculated via the equation of $D_{BD} = \frac{k_B T}{6\pi\mu R}$, in which k_B is the Boltzmann constant, T is the temperature in Kelvin, μ is the viscosity of the intestinal fluid (1×10^{-3} Pa*s), and R is the radius of the agent (Swartz and Fleury, 2007; Siggers et al., 2014; Yao et al., 2013). The thermophoresis diffusion coefficient D_{TP} is calculated via the equation of $D_{TP} = S_T D_{BD}$, in which S_T is the Soret coefficient (=0.01 Kelvin^{-1}). R_f is the retardation factor that has been defined as the ratio of the velocity of the solute (i.e., agent) to its solvent (i.e., interstitial fluid) (Jain, 1999; Boucher et al., 1998). In this study, R_f was used to reflect the effect of agent size on transportability. Briefly, R_f was calculated by comparing the average size of the agents and the pore size of the tissue extracellular matrix. If agents have a size much smaller than the pore size, R_f is close to 1. If the agent size is close to or larger than the pore size, R_f will significantly reduce. More detailed descriptions about how R_f was calculated in this study are provided in the supplementary materials.

2.3 Simulation of P_1 of ultrasound pressure wave

To improve the simulation speed, in this study, an analytical method was adopted to simulate the complex pressure amplitude P_1 (i.e., $P_1(r)$ in Equation 0a), which has been used in the literature for similar purposes (Prieur and Sapozhnikov, 2017; Sapozhnikov, 2012) and is expressed as Equation 5 in Table 1. In Equation 5, P_a is a scalar used to control the spatial peak amplitude value of $P_1(x, y, z)$ at the focal center, $z_d = ka^2/2$, $k = \frac{2\pi}{\lambda}$, λ is the ultrasound pressure wavelength, and a is a parameter affecting the lateral size of the beam in the plane $z = 0$. In this study, a was assigned a value equal to the lateral full-width-at-half-maximum (FWHM) of the ultrasound focus: $D_- = x^2 + y^2 + (z - jz_d)^2$, $D_+ = x^2 + y^2 + (z + jz_d)^2$, and $j = \sqrt{-1}$. In this study, the ultrasound frequency is 2.5 MHz, and the FWHM of the focus along the lateral (X and Y) and axial direction (Z, i.e., the wave propagation direction) is $\sigma_x = \sigma_y = 0.5$ and $\sigma_z = 3.5$ mm, respectively.

2.4 Numerical simulations

Readers may quickly realize that most of the equations in Table 1 involve a diffusion term (∇^2). In fact, Equations 1 is Poisson's equation. Equation 2b and 3 are diffusion equations, and Equation 4 is the continuity equation eventually involving two diffusion terms. This type of equation can be numerically solved by using a conventional finite difference method with appropriate initial and boundary conditions. When time is involved in the simulation, the stability condition has been well identified as $\Delta t < \frac{(\Delta l)^2}{2D}$. Here, Δt is the step size in time, and Δl is the step size in space. If a Cartesian coordinate system is adopted, Δl represents Δx, Δy, or Δz. D represents the diffusion coefficient, such as $k_t/\rho_0 c_t$ in Equation 3, when the diffusion equation has a format of $\frac{\partial F}{\partial t} = D\nabla^2 F$ (here F is a spatial and temporal variable). In this study, a Cartesian coordinate system was adopted. To show the data in the focal volume, the origin of the coordinate system was selected at the center of the ultrasound focus. When boundary conditions were needed, zero-gradient boundary conditions were adopted (i.e., $\frac{\partial F}{\partial l} = 0$, where l can be x, y, or z). This is reasonable because the boundaries

are far away from the ultrasound focus by adopting a simulation volume that is much bigger than the focal volume. In Equation 2a, the initial condition for $u_s = \int_0^{t_0} V_s dt$ was $u_s|_{t=0} = 0$, and its final value of $u_s|_{t=t_0} = u_{s0}$ was used as the initial condition for $\frac{\partial u_s}{\partial t} = KH\nabla^2 u_s$ in Equation 2b. Other initial conditions include $\Delta T = 0|_{t=0}$ and $C = C_0|_{t=0}$ (usually the concentration C is normalized by C_0).

3. Results and Discussion

3.1 "Squeezing" tissue's interstitial fluid out of the focal volume via ultrasound momentum transfer

Fig.2(a) shows the 2D distribution of the amplitude of the 1st-order ultrasound pressure wave (i.e., $|P_1| = \sqrt{R^2 + I^2}$) on the XZ(Y = 0) plane with a central peak value of $P_a = 1$ MPa (Sapozhnikov, 2012; Prieur and Sapozhnikov, 2017). The red box in Fig.2(a) indicates the focal area. The momentum transferred from the ultrasound wave to the tissue leads to the interstitial fluid being "splashed" away from the focal volume (Fig.2(c–d)). It further leads to an elevation of the hydrostatic pressure (P_{hs}) of the interstitial fluid. Meanwhile, the tissue solid matrix will be volumetrically compressed (data not shown). Fig.2(b) shows the distribution of the elevated fluid pressure P_{hs} on the XZ(Y = 0) plane induced by the ultrasound beam in Fig.2(a). Based on Darcy's law, P_{hs} will generate an exudation flow W_2 (Fig.2(c–d)). Thus, a small amount of tissue interstitial fluid will be squeezed out of the focal volume, which will also move the agents (i.e., the solutes in the fluid) out of the focal volume. Fig.2(c) shows the X and Y components of W_2 on the XY(Z = 0) plane. Fig.2(d) shows its X and Z components on XZ(Y = 0) plane. Each arrow points to the flow direction, and its length is proportional to the flow speed. The insets in Fig.2(c) and (d) display the magnitude of W_2 (i.e., $|W_2|$) on the XY(Z = 0) and XZ(Y = 0) plane, respectively. The velocity can reach as high as 0.25 microns/second in this example at the positions surrounding the center point, where the gradients of P_1 and P_{hs} (i.e., ∇P_1 and ∇P_{hs}) achieve the maxima. Note that P_{hs} is diffused in space because it is governed by a Poisson-like equation (i.e., Equation 1 in Table 1). Thus, the distribution of P_{hs} will be spatially expanded compared with that of $|P_1|$. This can be seen by comparing the lateral and axial FWHMs of P_{hs} in Fig.2(b) (3.6 and 10.5 mm) with those of $|P_1|$ in Fig.2(a) (0.5 and 3.5 mm), which may be favorable for transporting agents in a relatively large volume.

3.2 Backflows when ultrasound is off

Fig.3(a) shows the backflow velocity (W_2) on XY(Z = 0) plane at the time of 1 second after the ultrasound is off. The fluid is flowing back into the focal volume. Figs.3(c–d) show the corresponding spatial distribution of the magnitude of the backflow velocity ($|W_2|$) on the XY(Z = 0) and XZ(Y = 0) plane, respectively. Fig.3(b) displays the maximum backflow velocity as a function of time after the ultrasound is off. Clearly, the initial maximum velocity can reach as high as 1.8 microns/second and quickly reduces to 0.06 microns/second at t = 8.4 seconds. Then, the velocity decays slowly and remains a small value for a long time. This phenomenon of having a fast initial and a slow final relaxation speed is commonly seen in biological soft tissues after being compressed by an external force (Zhang

et al., 2008; Kwan et al., 1984; Ehlers and Markert, 2001). For safety, the mechanical index (MI) of the ultrasound should remain below the FDA-required safety threshold (MI<1.9) and the thermal indexes (TI) below the AIUM-required safety threshold (TI < 6; American Institute of Ultrasound in Medicine). Thus, this procedure can be safely repeated multiple times at each location when needed. The total amount of the squeezed-out agents will be accumulated. Because the size of the ultrasound focus is small, the spatial distribution of agents can be controlled by 3-dimensionally scanning a single focus or multiple foci generated via an array transducer.

3.3 Temperature rise induced by ultrasound

As an example, Fig.4 shows the change of ΔT as a function of time at the center of the ultrasound focus with an exposure time of t_0 = 10 seconds and an ultrasound spatial peak amplitude P_a = 1 MPa and α = 0.58 db/MHz/cm (for soft tissues). Clearly, during the period between 0 and 10 seconds when the ultrasound is turned on, ΔT quickly rises from 0 to 4.87°C, but the increase rate is gradually reducing due to thermal diffusion and blood perfusion (see the first term and the second term on the right hand side of Equation 3a in Table 1). The inset shows the 2D distribution of ΔT on the XZ(Y = 0) plane when t = t_0 = 10 seconds. The lateral (X) and axial (Z) FWHMs of ΔT are 1.4 and 6.5 mm, respectively, which are wider than those of $|P_1|$ in Fig.2(a) (0.5 and 3.5 mm, respectively) due to the existing of thermal diffusion.

3.4 Concentration change induced by ultrasound

In this section, both temperature-insensitive and -sensitive agents are investigated. Here, a temperature-insensitive agent means the temperature change does not affect the size or other transport-related parameters. Conversely, a temperature-sensitive agent (such as a USF agent in this study) indicates the diameter of the agent significantly reduces when temperature is above its phase transition threshold, and it recovers when temperature falls below the threshold.

3.4.1 Temperature-insensitive agents: For simulation simplicity, both agents and tissue pores are assumed to be spherical, and their diameters are assumed to have Gaussian distributions (not required). The standard deviations of the diameter distributions are arbitrarily selected to be 25% of their average diameters (not required). For example, if the average diameters of the agent and the tissue pore size are set as 40 and 80 nm, respectively, and the 25% standard deviation of their diameter distributions are 10 and 20 nm, respectively, then the majority of the nanoparticles will have a size smaller than that of the majority of the pores. Therefore, they should be able to pass through the pores without significant resistance. Whenever the following parameters are constant, their values will be set as follows: the spatial peak pressure value is P_a = 0.8 MPa; the ultrasound exposure time is t_0 = 40 seconds; based on the above two parameters, the spatial peak temperature increases ΔT = 4.15°C if the tissue ultrasound absorption coefficient is α = 0.58 db/MHz/cm; the hydraulic conductivity is K=4x10^{-14} m^4/N/S (Liu and Schlesinger, 2015); the apparent module is H=1 MPa (Zhang et al., 2008; Kwan et al., 1984; Ehlers and Markert, 2001). The values of the parameters used in simulation are found from literature mainly for soft tissues (such as breast) or related tumors.

Figs.5(a–b) show the change of the normalized concentration of the agent (C/C_0) on XY(Z = 0) and XZ(Y = 0) planes at the time right after the ultrasound is off, respectively (i.e., t = t_0 = 40 seconds). Figs.5(c–d) show the results at the time of 60 seconds after ultrasound is turned off (i.e., t=t_0+60=100 seconds). Figs.5(e–f) plot the normalized concentration changes along X and Z directions, respectively, at different times. Fig.5(g) shows the dynamic change of the normalized concentration as a function of time at the ultrasound focal center with different agent average diameters. Fig.5(h) displays the variation rates of the normalized concentration caused by different mechanisms: diffusion (i.e., $\nabla \bullet [(D_{BD} \nabla C)]$), thermophoresis (i.e., $\nabla \bullet [C D_{TP} \nabla (\Delta T)]$, and ultrasound-induced convection rate (i.e., $-\nabla \bullet [C R_f W_2]$). Figs.5(i–j) show the effect of the tissue apparent module (H) on the relaxation of the normalized concentration change at the center of the focus after ultrasound is off. The agent average diameter is 1.6 nm and 80 nm in Fig.5(i) and (j), respectively. Fig.5(k) displays the effect of the agent average diameter on the normalized concentration at t = 40 and 100 seconds.

From the above results, it can be seen that during the period when the ultrasound is on ($0 \leq t \leq 40$ seconds), the agents are continuously squeezed out of the focal volume as shown in Figs.5(a–g). The concentration in the surrounding areas should increase (i.e., $C/C_0 > 1$), but it may not be visible in Figs.5(a–b) because of the large surrounding volume. The maximum concentration reduction at the center of the ultrasound focus can reach ~4.5% (i.e., reduced from 100% to 95.5%) at t = 40 seconds for the agent with a diameter of 10 nm as shown in Fig.5(g). Other agents with a diameter smaller than the pore diameter of 80 nm (such as 40, 4, 1.5 nm) can also achieve a similar concentration change. This is understandable because these nanoagents have the similar R_f due to their small size. In the group in which the agent size is smaller than tissue pore size, the agent with 1.5 nm has slightly smaller concentration reduction than those of other agents, and it also has a quicker recovery speed after ultrasound is off. This is mainly because of the relatively large diffusion caused by concentration gradient due to its much smaller size. However, when the agent size is much larger than the pore size, such as 120-300 nm, the maximum concentration change is less than 1% because of the high resistance of tissue to the large agents. Fig.5(h) shows that the SIF-TUM contribution (the red line) is much more significant than those from the diffusion and thermophoresis. Therefore, SIF-TUM is the dominant driving force of the nanoagent transport. During the period when the ultrasound is on (0-40 seconds), the rate induced by SIF-TUM is negative, which means the concentration in the ultrasound focal volume will be reduced. Once the ultrasound exposure is stopped at 40 seconds, the rate becomes positive, which means the fluid flows back into the focal volume. Also, during the period when the ultrasound is on, the SIF-TUM rate is almost a constant, as shown in Fig.5(h), although it is slightly reduced because the remaining fluid in the focal volume is slowly reduced when fluid is continuously squeezed out. Therefore, the concentration is approximately reduced linearly as a function of time during this period as shown in Fig.5(g). After the ultrasound is off, the normalized concentration (C/C_0) quickly recovers, reaching a relatively stable value and then decaying extremely slowly, which is shown in Fig.5(g). This can be understood by examining the backflow rate on Fig.5(h). After the ultrasound is off, the backflow rate mainly depends on the tissue property and becomes independent of the ultrasound parameter. The initial rate of the backflow is even greater than the flow rate

induced by the ultrasound during the period of ultrasound illumination. However, it quickly decays to a small number (because of the reduction of $\nabla^2 u_s$ with the solid tissue recovery), as shown in Fig.5(h), leading to a slow recovery of the concentration of the agents, as shown in Fig.5(g). This is a typical phenomenon in bi-phase materials. Based on Figs.5(e–h), the high initial backflow speed (i.e., immediately after the ultrasound is off) leads to a small portion of concentration recovery in the focal volume. However, when t > 50 seconds, the backflow speed becomes so small that the agent concentration recovery is almost unnoticeable during the time frame adopted in this study (except for the small agents, such as 1.5 and 4 nm in diameter). Another interesting phenomenon is that a ring shape of concentration is observed in Figs.5(c–d and e–f), which means that more agents are accumulated surrounding the focal area after the ultrasound is turned off. The exact reason for the forming of this ring shape distribution is unknown. However, we speculate that this may be caused by the initially fast and finally slow backflows, and it may be further related to the spatial phase difference of the backflows between the central and surrounding area of the ultrasound focus.

Figs.5(i–j) indicates the tissue relaxation is also slightly affected by the apparent modulus (H). Obviously, the higher H provides the higher initial speed of backflows and reaches the final value more quickly. Again, the continuous concentration reduction at the late stage in Fig.5(i) is mainly due to the diffusion of the small agent, which is much weaker for large agents as shown in Fig.5(j). Fig.5(k) displays how the agent diameter affects the normalized concentration change (C/C_0) at the ultrasound focal center. The red line with circles and the blue line with squares are the values at t = 40 and t = 100 seconds, respectively. Clearly, agents with a diameter between 10 and 40 nm achieve the optimized concentration reduction when the average diameter of the tissue pores is 80 nm. This means that within this diameter range, the agents not only freely pass through the tissue pores but also avoid significant natural diffusion due to their medium size. When the diameter is larger than 40 nm (especially larger than 80 nm), the resistance of tissue to the agent transport becomes significant, and the concentration change becomes difficult. On the other hand, when the diameter is smaller than 10 nm, although these agents can easily pass through the pores, they can also diffuse back into the focal volume more efficiently than the larger ones, which reduces the efficiency of concentration change. However, even with this disadvantage of diffusion-caused backflow for small-sized agents (such as 1.5 and 4 nm), their concentration changes are still higher than those of the large-sized agents (such as >80 nm). This means the transportability is more critical than the diffusivity in the current setup.

Fig.6 shows three examples about how the concentration is changed when multiple ultrasound foci exist. Fig.6(a) displays the normalized concentration distribution on the XY(Z = 0) plane when a total of 16 ultrasound foci exist (which may be achieved via either a fast scanning or an array transducer simultaneously generating multiple foci). The red dots indicate the focus locations. The concentration in the scanned area is reduced, and the agents are pushed outside the focal area. This may provide a unique capability to control the agent distribution externally. Figs.6(b)–(c) display the similar results but with two random distributions of the foci (or scans). The concentration of the agents can clearly be controlled by selecting the scanning area. The adopted parameters are similar to those in Figure 5,

including diameter = 40 nm; P_a = 0.8 MPa; t_0 = 40 seconds; H = 1 MPa; ΔT = 4.15°C; K = 4x10^{-14} m^4/N/S; and FWHM = 0.5, 0.5, and 3.5 mm along X, Y, and Z, respectively.

3.4.2 Temperature-sensitive agents (such as USF imaging contrast agents):

The motivation of investigating temperature-sensitive agents in this study comes from our USF imaging. Usually, the diameters of USF agents can reduce ~2 times when the environment temperature is increased above a temperature threshold of the agents (i.e., the lower critical solution temperature of the material, LCST, which is set as 38°C in this study, whereas the tissue background temperature is 37°C). Thus, when the ultrasound is applied and tissue temperature in the focal volume is raised by a few degrees (at a timescale of a few hundreds of milliseconds in USF imaging or seconds to minutes in SIF-TUM), the agents in the focal volume will shrink quickly (at a timescale from microseconds to milliseconds (Zhang et al., 2009; Podewitz et al., 2019; Bentley, 2010). The size reduction leads to the increase of R_f, which is favorable for the agents to be transported via the SIF-TUM-induced flow. After the agents are squeezed out, the agents will expand to their original size. This leads to the reduction of R_f, which is unfavorable for agents to flow back after the ultrasound is off. Compared with temperature-insensitive agents, this feature may be favorable for enhancing the transport efficiency and may make the transport possible for agents with a size larger than the pore size.

Similar to Fig.5, Fig.7 shows the corresponding results for temperature-sensitive agents. Figs.7(a) and (b) show the 2D distribution of the normalized concentration on XY(Z = 0) and XZ(Y = 0) planes, respectively, right after ultrasound is off (t = t_0 = 40 seconds). Figs.7(c) and (d) display similar results when t = 100 seconds. Figs.7(e–f) show the 1D distribution of normalized concentration along the X and Z directions at different times, respectively. The major difference is that the average diameter of the agent in Figs.7(a–f) is 80 nm, whereas it is 40 nm in Figs.5(a–f). Compared Figs.7(a–f) with Figs.5(a–f), concentration changes are evidently similar in the two situations. Therefore, using a temperature-sensitive agent allows using an agent with a larger size to achieve similar performance in concentration change compared with using a temperature-insensitive agent. This is beneficial for improving delivery efficiency because a larger-sized agent will have a bigger volume and payload capacity (such as for drugs, proteins, molecules). Fig.7(g) plots the dynamic variation of the normalized concentration at the focal center as a function of time for agents with different diameters. Compared Fig.7(g) with Fig.5(g), for the same agent diameter, the concentration change is higher for temperature-sensitive agents than for temperature-insensitive agents. For further quantitative comparison of the concentrations in Fig.7(g) and Fig.5(g), the normalized concentrations were selected at two time points, t = 40 and 100 seconds, and they were plotted as a function of the agent diameter in Fig.7(h). Obviously, the curve for the temperature-sensitive agents acquired at t = 40 seconds (the red line with circles) is shifted toward the right-hand side compared with that for the temperature-insensitive agents (the blue line with triangles). Similar results can also be found for data acquired at t = 100 seconds by comparing the pink line with squares with the green line with triangles. The vertical dotted line indicates that the tissue pore size is 80 nm. As discussed before, the optimized agent size for temperature-insensitive agents should be between 10 and 40 nm for balancing transportability and diffusivity. Fortunately,

the optimized agent size for temperature-sensitive agents is widely broadened and can reach a range between 10 and 120 nm (see the red line with circles and the pink line with squares). It is important to note that when a USF agent is shrunk at a high-temperature environment, it usually expels water molecules out of the agent instead of the payloads. This feature provides a great opportunity to allow transporting large-sized agents (such as 40-120 nm) in tissue using this SIF-TUM technology combined with temperature-sensitive agents. Otherwise, it will be extremely difficult to transport such big agents. Fig.7(i) further plots the difference of the normalized concentration between the temperature-sensitive and -insensitive agents as a function of agent diameter. When the diameter is ≤40 nm or ≥300 nm, both types of agents have similar concentration changes. This is understandable because when the agent has a size either much smaller or much bigger than the tissue pore size, the transportability of the agent is much less dependent on the size. However, when the agent has a size close to or slightly above the pore size (such as 80-200 nm in this example), the feature of thermally reducing size can help improve transportability. This can be seen from Fig.7(i), in which the difference of the concentration change between the two types of agents is obvious for agents with a size between 80 and 200 nm. This result indicates that if the agent size is within the range of 80-200 nm, using a temperature-sensitive agent should have a higher transportability than using a temperature-insensitive agent. However, when temperature-sensitive agents have been selected, using a size within the optimized range of 10–120 nm is a better choice compared with using an agent with a size >120 nm because the absolute value of the concentration change is higher. Fig.7(j) shows the effect of the apparent module on the tissue recovery rate. The same result as Fig.5(j) can be drawn that the higher H will lead to a faster initial recovery rate. In addition, Fig.7(j) shows a higher concentration change than Fig.5(j). This further indicates that a temperature-sensitive agent has a higher transportability than a temperature-insensitive agent if the agent diameter is appropriate.

3.5 Further discussions about the fluid dynamics of SIF-TUM

3.5.1 Peclet number (*Pe*):

Pe is a non-dimensional number and used to compare the contributions from convection (i.e., SIF-TUM) and diffusion. It is defined as $Pe = LW_2/D_{BD}$ in which L is the characteristic length (0.25 mm, the half of the lateral focal size of the ultrasound focus in this study), W_2 is the flow velocity induced by SIF-TUM ($1\ \mu m/s$) and D_{BD} is the diffusion coefficient (calculated via $\frac{k_B T}{6\pi\mu R} = 5.49*10^{-12}\ m^2/s$, in which $T = 37\ C^0,\ \ R = 40\ nm,\ \mu = 1*10^{-3}\ Pa*s$). Thus, one can have $Pe \approx 45.5$, which is great than 1 and means the contribution from the convection is significantly higher than that from the diffusion. This is in agreement with the conclusion from Fig.5(h). Right after the ultrasound is off, the initial backflow velocity is high but quickly reduces as indicated by Fig.5(h). Thus, one can use the above equation to calculate Pe by simply changing the velocity W_2. When the velocity is so small that the diffusion becomes the dominant mechanism, Pe will be smaller than 1 eventually.

3.5.2 Reynolds number (*Re*):

Reynolds number of the interstitial fluid flow in tissue is usually very small and ignorable as indicated in the literature (Yao et al., 2012). It is ~$0.25*10^{-3}$ based on the equation of

$Re = (\rho W_2 L)/\mu = 1000\left(\frac{kg}{m^3}\right)*1\left(\frac{\mu m}{s}\right)*0.25(mm)/10^{-3}(Pa * s)$. This means the inertia force is neglected. Thus, Darcy's law is frequently used. In fact, in our studies the Darcy's law describes a macroscopic streaming, which is statistically formed by numerous microscopic streaming in tissue.

3.5.3 A diffusion wave vs an elastic wave: The key equations in this study are either Poisson's or diffusion equations. This is mainly because the 2nd-order derivative term relative to time (i.e., the inertia term) is ignored. However, if one repeatedly compresses and relaxes the tissue using ultrasound at a certain frequency, it may generate a fluid oscillation. This type of oscillation may be partially similar to a diffusion wave (Mandelis, 2000) (because the Equation 1 is a Poisson's equation and the Equation 2 is a diffusion equation), which is different from an elastic wave described by a wave equation.

3.6 Limitations

3.6.1 Zero source and sink: In this study, the source (σ_s) and sink (σ_i) rates of nanoagents are assumed to be zero. This situation is suitable for the following scenarios: (1) nanoagent distribution in blood vessels and intertidal space has reached a balance, which usually happens sometime after a bolus intravenous injection; (2) nanoagents are intratumorally injected; (3) the timescale of SIF-TUM at each location is at seconds or minutes. In such a short time window, the amount of nanoagents uptake by cells may not be significant. However, in practice it is possible that the source or sink rates may not be zero. For example, the concentration of nanoagents in blood may be high at the early stage after a bolus intravenous injection, and the exchange of nanoagents from the capillary network to the interstitial space may exist. Also, nanoagents may be cleaned by cells or lymphatic system at a much shorter timescale than that of the SIF-TUM. If these sources and sinks cannot be ignored, they can be considered via a non-zero σ_s and σ_i.

3.6.2 The effects of tissue heterogeneities, nanoagent properties and ultrasound shear wave: In this study, models only consider two tissue compartments, interstitial fluid and solid matrix. The effect of blood vessel network, osmotic pressure, and other tissue heterogeneities are not included. Besides the size, other nanoagent properties, such as shape and surface charges, may also affect the transport efficiency, which have been ignored in this study. In addition, only the 1st-order longitudinal progressive ultrasound wave is considered in this study via an analytical method. Ultrasound reflection, scattering, share wave, and non-linear effect in tissue have been ignored. The major reason is to focus on the dominant effects so that the model can be simple and easy to understand, and the total number of unknown parameters needed in the simulation can be reduced. It may be helpful to consider these effects in future when needed so that the models can be more accurate.

4. Conclusions

In this study, the feasibility of using a focused ultrasound beam to induce interstitial fluid streaming in deep tissue via momentum transfer between the ultrasound wave and tissue interstitial fluid has been investigated. Biological tissue is considered a bi-phase medium including both a fluid and a solid matrix. The interaction between the ultrasound and the

two components (i.e., fluid and solid) has been modeled and investigated via numerical simulations. Both mechanical and thermal effects induced by the ultrasound have been considered in the models. The results show that it is highly feasible to induce a macroscopic fluid streaming with a peak velocity at the level of microns/second in a focal zone at a level of millimeters. The streaming mechanism is found to be that the ultrasound wave transfers its momentum to tissue fluid, which leads to a "splashing" of the fluid out of the focal volume. Because of the finite value of tissue hydraulic conductivity, the "splashed" fluid further leads to the elevation of the hydrostatic pressure in the focal volume. This elevated hydrostatic pressure can generate a macroscopic exudation flow. The entire procedure can be imagined as a scenario that the ultrasound squeezes the tissue in the focal volume along all three dimensions (X, Y, and Z). The velocity of this exudation flow is found to be determined by a term of $[\nabla P_1 \bullet \nabla P_1^*]$, which is the dot product between the gradient of the 1st-order ultrasound pressure wave and its complex conjugate, rather than the ultrasound pressure itself. Furthermore, after the ultrasound is off, the fluid can backflow into the focal volume due to the tissue elasticity of the solid matrix. The speed of the recovery of the fluid (or solid matrix) right after the ultrasound is off is usually high because of the large compression of the solid matrix and high apparent modulus. This speed decays quickly as time goes on because of the rapid expansion of the solid matrix, so it takes a much longer time for the rest of the fluid to flow back. This phenomenon provides a unique opportunity to control the fluid and the agents that are dissolved in the fluid. In this study, this technology is named squeezing interstitial fluid via the transfer of ultrasound momentum (SIF-TUM). The simulation results indicate that it is highly possible to externally accelerate agent transport in deep tissue and further control the nanoagent distribution by adopting appropriate experimental conditions. The mechanism of SIF-TUM is different from the ARF-based and ultrasound-enhanced drug delivery technologies. The success of this technology may significantly improve the delivery efficiency and the related therapeutic or diagnostic efficiency. It can even possibly make a local injection (whenever possible) more attractive than a systemic injection because of its low toxicity and high delivery efficiency.

Supplementary Material

Refer to Web version on PubMed Central for supplementary material.

Acknowledgement

This work was financially supported in part by funding from the NIH/NIBIB 1R15EB030809-01, the REP 270089, and the CPRIT RP170564. I would like to also appreciate my family members for their strong support so that I could have enough time during the past two years to complete this work.

References

Aglyamov S, Karpiouk AB, Linskii Y, Zabolotskaya E and Emelianov S 2007 Motion of a solid sphere in a viscoelastic medium in response to applied acoustic radiation force: Theoretical analysis and experimental verification The Journal of the Acoustical Society of America 122 1927–36 [PubMed: 17902829]

Anand A and Kaczkowski PJ 2008 Noninvasive measurement of local thermal diffusivity using backscattered ultrasound and focused ultrasound heating Ultrasound in medicine & biology 34 1449–64 [PubMed: 18450361]

Barua S and Mitragotri S 2014 Challenges associated with penetration of nanoparticles across cell and tissue barriers: A review of current status and future prospects Nano Today 9 223–43 [PubMed: 25132862]

Baxter LT and Jain RK 1989 Transport of fluid and macromolecules in tumors. I. Role of interstitial pressure and convection Microvasc Res 37 77–104 [PubMed: 2646512]

Bentley CD 2010 The Phase Transition of Poly(N-Isopropylacrylamide). (Ann Arbor: The University of Liverpool (United Kingdom)) p 193

Boucher Y, Brekken C, Netti PA, Baxter LT and Jain RK 1998 Intratumoral infusion of fluid: estimation of hydraulic conductivity and implications for the delivery of therapeutic agents British Journal of Cancer 78 1442–8 [PubMed: 9836476]

Bruus H 2011 Acoustofluidics 1: Governing equations in microfluidics Lab on a Chip 11 3742–51 [PubMed: 22011885]

Bruus H 2012a Acoustofluidics 2: Perturbation theory and ultrasound resonance modes Lab on a Chip 12 20–8 [PubMed: 22105715]

Bruus H 2012b Acoustofluidics 7: The acoustic radiation force on small particles Lab on a Chip 12 1014–21 [PubMed: 22349937]

Cheng BB, Bandi V, Wei MY, Pei YB, D'Souza F, Nguyen KT, Hong Y and Yuan BH 2016 High-Resolution Ultrasound-Switchable Fluorescence Imaging in Centimeter-Deep Tissue Phantoms with High Signal-To-Noise Ratio and High Sensitivity via Novel Contrast Agents Plos One 11

Curra FP, Mourad PD, Khokhlova VA, Cleveland RO and Crum LA 2000 Numerical simulations of heating patterns and tissue temperature response due to high-intensity focused ultrasound IEEE Transactions on Ultrasonics, Ferroelectrics, and Frequency Control 47 1077–89 [PubMed: 18238643]

de Smet M, Heijman E, Langereis S, Hijnen NM and Grüll H 2011 Magnetic resonance imaging of high intensity focused ultrasound mediated drug delivery from temperature-sensitive liposomes: An in vivo proof-of-concept study Journal of Controlled Release 150 102–10 [PubMed: 21059375]

Deckers R and Moonen CTW 2010 Ultrasound triggered, image guided, local drug delivery Journal of Controlled Release 148 25–33 [PubMed: 20709123]

Doherty JR, Trahey GE, Nightingale KR and Palmeri ML 2013 Acoustic radiation force elasticity imaging in diagnostic ultrasound IEEE Transactions on Ultrasonics, Ferroelectrics, and Frequency Control 60 685–701 [PubMed: 23549529]

Dromi S, Frenkel V, Luk A, Traughber B, Angstadt M, Bur M, Poff J, Xie J, Libutti SK, Li KCP and Wood BJ 2007 Pulsed-High Intensity Focused Ultrasound and Low Temperature–Sensitive Liposomes for Enhanced Targeted Drug Delivery and Antitumor Effect Clin Cancer Res 13 2722 [PubMed: 17473205]

Duhr S and Braun D 2006 Why molecules move along a temperature gradient Proceedings of the National Academy of Sciences 103 19678–82

Eckart C 1948 Vortices and Streams Caused by Sound Waves Physical Review 73 68–76

Ehlers W and Markert B 2001 A Linear Viscoelastic Biphasic Model for Soft Tissues Based on the Theory of Porous Media Journal of Biomechanical Engineering 123 418–24 [PubMed: 11601726]

El Ghamrawy A, de Comtes F, Koruk H, Mohammed A, Jones JR and Choi JJ 2019 Acoustic Streaming in a Soft Tissue Microenvironment Ultrasound in Medicine & Biology 45 208–17 [PubMed: 30336964]

Frenkel V 2008 Ultrasound mediated delivery of drugs and genes to solid tumors Adv Drug Deliver Rev 60 1193–208

Grüll H and Langereis S 2012 Hyperthermia-triggered drug delivery from temperature-sensitive liposomes using MRI-guided high intensity focused ultrasound Journal of Controlled Release 161 317–27 [PubMed: 22565055]

Hancock H, Smith L, Cuesta J, Durrani A, Angstadt M, Palmeri M, Kimmel E and Frenkel V 2009 Investigations into Pulsed High-Intensity Focused Ultrasound–Enhanced Delivery: Preliminary

Evidence for a Novel Mechanism Ultrasound in Medicine & Biology 35 1722–36 [PubMed: 19616368]

Jain RK 1999 Transport of Molecules, Particles, and Cells in Solid Tumors Annu Rev Biomed Eng 1 241–63 [PubMed: 11701489]

Kwan MK, Michael Lai W and Van Mow C 1984 Fundamentals of fluid transport through cartilage in compression Annals of Biomedical Engineering 12 537–58 [PubMed: 6534222]

Lee ES, Lee JY, Kim H, Choi Y, Park J, Han JK and Choi BI 2013 Pulsed high-intensity focused ultrasound enhances apoptosis of pancreatic cancer xenograft with gemcitabine Ultrasound in Medicine & Biology 39 1991–2000 [PubMed: 23972483]

Leunig M, Yuan F, Menger MD, Boucher Y, Goetz AE, Messmer K and Jain RK 1992 Angiogenesis, microvascular architecture, microhemodynamics, and interstitial fluid pressure during early growth of human adenocarcinoma LS174T in SCID mice Cancer Res 52 6553–60 [PubMed: 1384965]

Lighthill SJ 1978 Acoustic streaming Journal of Sound and Vibration 61 391–418

Liu LJ and Schlesinger M 2015 Interstitial hydraulic conductivity and interstitial fluid pressure for avascular or poorly vascularized tumors Journal of Theoretical Biology 380 1–8 [PubMed: 25986434]

Liu R, Yao T, Liu Y, Yu S, Ren L, Hong Y, Nguyen KT and Yuan B 2020a Temperature-sensitive polymeric nanogels encapsulating with β-cyclodextrin and ICG complex for high-resolution deep-tissue ultrasound-switchable fluorescence imaging Nano Research 13 1100–10

Liu Y, Yao T, Cai W, Yu S, Yi H, Nguyen K and Yuan B 2020b A Biocompatible and Near-Infrared Liposome for In Vivo Ultrasound-Switchable Fluorescence Imaging Advanced Healthcare Materials 9 1901457

Løvmo MK, Yemane PT, Bjørkøy A, Hansen R, Cleveland RO, Angelsen BA and Davies C d L 2021 Effect of Acoustic Radiation Force on Displacement of Nanoparticles in Collagen Gels IEEE Transactions on Ultrasonics, Ferroelectrics, and Frequency Control 68 416–31 [PubMed: 32746200]

Mandelis A 2000 Diffusion Waves and their Uses Physics Today 53 29–34

McNamara K and Tofail SAM 2017 Nanoparticles in biomedical applications Advances in Physics: X 2 54–88

Netti PA, Baxter LT, Boucher Y, Skalak R and Jain RK 1995 Time-dependent behavior of interstitial fluid pressure in solid tumors: implications for drug delivery Cancer Res 55 5451–8 [PubMed: 7585615]

O'Neill BE, Vo H, Angstadt M, Li K, Quinn T and Frenkel V 2009 Pulsed High Intensity Focused Ultrasound Mediated Nanoparticle Delivery: Mechanisms and Efficacy in Murine Muscle Ultrasound in Medicine & Biology 35 416–24 [PubMed: 19081668]

Park SM, Kim MS, Park S-J, Park ES, Choi K-S, Kim Y-s, Kim HR 2013 Novel temperature-triggered liposome with high stability: Formulation, in vitro evaluation, and in vivo study combined with high-intensity focused ultrasound (HIFU) Journal of Controlled Release 170 373–9 [PubMed: 23770213]

Pei YB, Wei MY, Cheng BB, Liu Y, Xie ZW, Nguyen K and Yuan BH 2014 High resolution imaging beyond the acoustic diffraction limit in deep tissue via ultrasound-switchable NIR fluorescence Sci Rep-Uk 4 4690

Pitt WG 2008 Ultrasound in Drug and Gene Delivery Adv Drug Deliver Rev 60 1095–6

Podewitz M, Wang Y, Quoika PK, Loeffler JR, Schauperl M and Liedl KR 2019 Coil–Globule Transition Thermodynamics of Poly(N-isopropylacrylamide) The Journal of Physical Chemistry B 123 8838–47 [PubMed: 31545046]

Prieur F and Sapozhnikov OA 2017 Modeling of the acoustic radiation force in elastography The Journal of the Acoustical Society of America 142 947–61 [PubMed: 28863603]

Raghavan R 2018 Theory for acoustic streaming in soft porous matter and its applications to ultrasound-enhanced convective delivery Journal of therapeutic ultrasound 6 6 [PubMed: 30083324]

Ramanujan S, Pluen A, McKee TD, Brown EB, Boucher Y and Jain RK 2002 Diffusion and Convection in Collagen Gels: Implications for Transport in the Tumor Interstitium Biophysical Journal 83 1650–60 [PubMed: 12202388]

Ranjan A, Jacobs GC, Woods DL, Negussie AH, Partanen A, Yarmolenko PS, Gacchina CE, Sharma KV, Frenkel V, Wood BJ and Dreher MR 2012 Image-guided drug delivery with magnetic resonance guided high intensity focused ultrasound and temperature sensitive liposomes in a rabbit Vx2 tumor model Journal of Controlled Release 158 487–94 [PubMed: 22210162]

Sapozhnikov OA 2012 An exact solution to the Helmholtz equation for a quasi-Gaussian beam in the form of a superposition of two sources and sinks with complex coordinates Acoustical Physics 58 41–7

Sarvazyan A, Rudenko O and Nyborg W 2010 Biomedical Applications of Radiation Force of Ultrasound: Historical Roots and Physical Basis Ultrasound in Medicine & Biology 36 1379–94 [PubMed: 20800165]

Sarvazyan A, Rudenko O, Swanson S, Fowlkes JB and Emelianov SY 1998 Shear wave elasticity imaging: a new ultrasonic technology of medical diagnostics Ultrasound in Medicine & Biology 24 1419–35 [PubMed: 10385964]

Shi J, Kantoff PW, Wooster R and Farokhzad OC 2017 Cancer nanomedicine: progress, challenges and opportunities Nature Reviews Cancer 17 20–37 [PubMed: 27834398]

Siggers JH, Leungchavaphongse K, Ho CH and Repetto R 2014 Mathematical model of blood and interstitial flow and lymph production in the liver Biomechanics and Modeling in Mechanobiology 13 363–78 [PubMed: 23907149]

Soares S, Sousa J, Pais A and Vitorino C 2018 Nanomedicine: Principles, Properties, and Regulatory Issues Frontiers in Chemistry 6

Soneson JE 2009 A User-Friendly Software Package for HIFU Simulation AIP Conference Proceedings 1113 165–9

Swartz MA and Fleury ME 2007 Interstitial Flow and Its Effects in Soft Tissues Annu Rev Biomed Eng 9 229–56 [PubMed: 17459001]

Tebebi PA, Kim SJ, Williams RA, Milo B, Frenkel V, Burks SR and Frank JA 2017 Improving the therapeutic efficacy of mesenchymal stromal cells to restore perfusion in critical limb ischemia through pulsed focused ultrasound Sci Rep-Uk 7 41550

Vyas R and Rustgi ML 1992 Green's function solution to the tissue bioheat equation Medical Physics 19 1319–24 [PubMed: 1435617]

Wongsuwarn S, Vigolo D, Cerbino R, Howe AM, Vailati A, Piazza R and Cicuta P 2012 Giant thermophoresis of poly(N-isopropylacrylamide) microgel particles Soft Matter 8 5857–63

Wu J 2018 Acoustic Streaming and Its Applications Fluids 3 108

Yao T, Liu Y, Ren L and Yuan B 2021 Improving sensitivity and imaging depth of ultrasound-switchable fluorescence via an EMCCD-gain-controlled system and a liposome-based contrast agent Quantitative imaging in medicine and surgery 11 957–68 [PubMed: 33654669]

Yao T, Yu S, Liu Y and Yuan B 2019 In vivo ultrasound-switchable fluorescence imaging Sci Rep-Uk 9 9855

Yao W, Li Y and Ding G 2012 Interstitial Fluid Flow: The Mechanical Environment of Cells and Foundation of Meridians Evidence-Based Complementary and Alternative Medicine 2012 853516 [PubMed: 23365601]

Yao W, Shen Z and Ding G 2013 Simulation of Interstitial Fluid Flow in Ligaments: Comparison among Stokes, Brinkman and Darcy Models International Journal of Biological Sciences 9 1050–6 [PubMed: 24250250]

Yu S, Wang Z, Yao T and Yuan B 2020a Near-infrared temperature-switchable fluorescence nanoparticles Quantitative imaging in medicine and surgery 11 1010–22

Yu S, Yao T, Liu Y and Yuan B 2020b In vivo ultrasound-switchable fluorescence imaging using a camera-based system Biomed Opt Express 11 1517–38 [PubMed: 32206426]

Yuan B, Uchiyama S, Liu Y, K. NT and Alexandrakis G 2012 High-resolution imaging in a deep turbid medium based on an ultrasound-switchable fluorescence technique Appl Phys Lett 101 033703 [PubMed: 22893732]

Yuh EL, Shulman SG, Mehta SA, Xie J, Chen L, Frenkel V, Bednarski MD and Li KCP 2005 Delivery of Systemic Chemotherapeutic Agent to Tumors by Using Focused Ultrasound: Study in a Murine Model Radiology 234 431–7 [PubMed: 15671000]

Zhang S-h, Chen Y, Li H and Weng Y-x 2009 Transitional Process of Ploy(N-isopropylacrylamide) in Deuterated Solution Chinese Journal of Chemical Physics 22 447–52

Zhang Y, Czerwonka L, Tao C and Jiang JJ 2008 A biphasic theory for the viscoelastic behaviors of vocal fold lamina propria in stress relaxation The Journal of the Acoustical Society of America 123 1627–36 [PubMed: 18345850]

Ziadloo A, Xie J and Frenkel V 2013 Pulsed focused ultrasound exposures enhance locally administered gene therapy in a murine solid tumor model The Journal of the Acoustical Society of America 133 1827–34 [PubMed: 23464051]

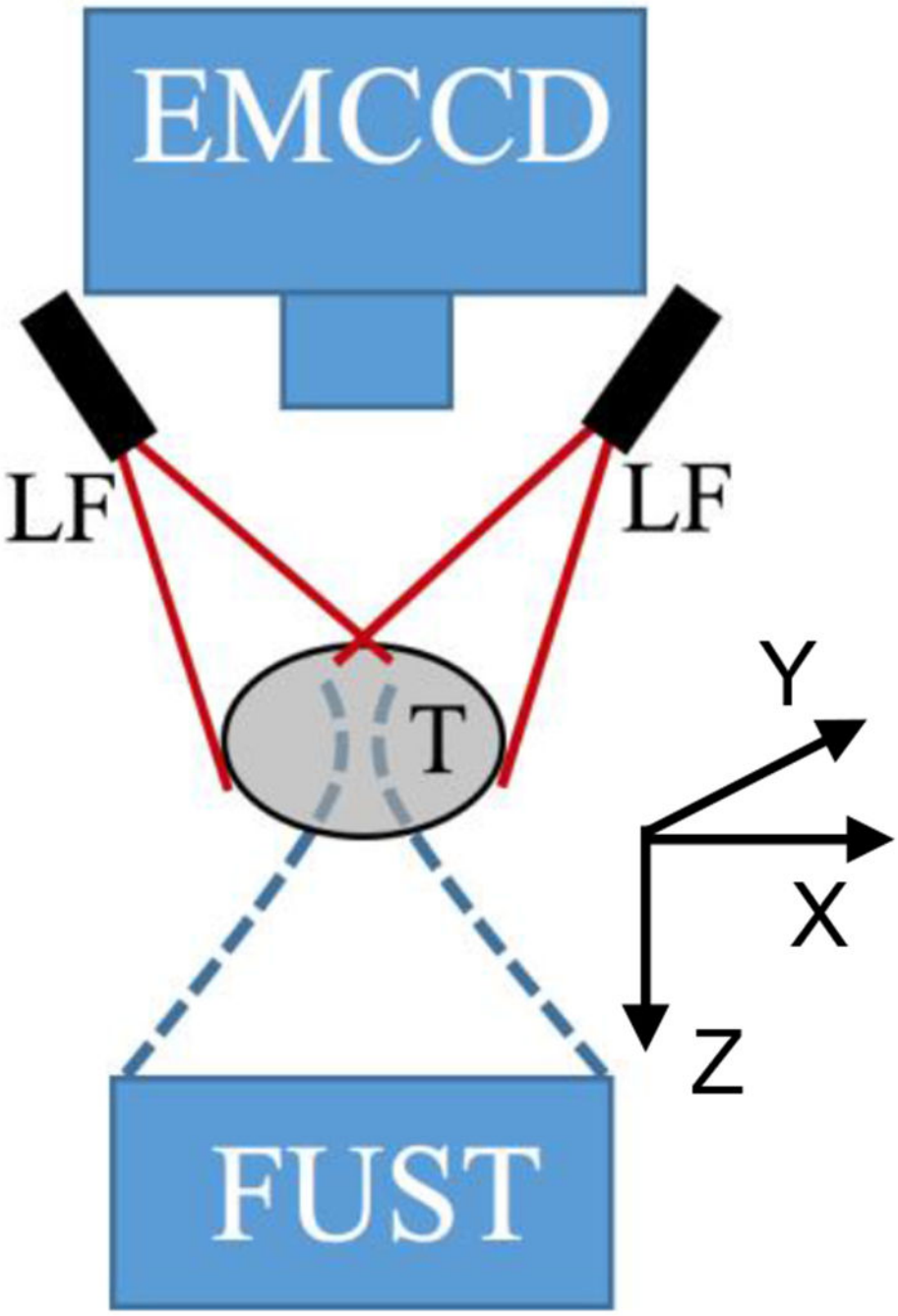

Fig.1:
A commonly used setup in USF imaging to help understand SIF-TUM, including four major components: focused ultrasound transducer (FUST), tumor (T), two excitation light fibers (LF), a camera (EMCCD). The X and Y directions are called horizontal or lateral directions, and the Z direction is axial or depth direction.

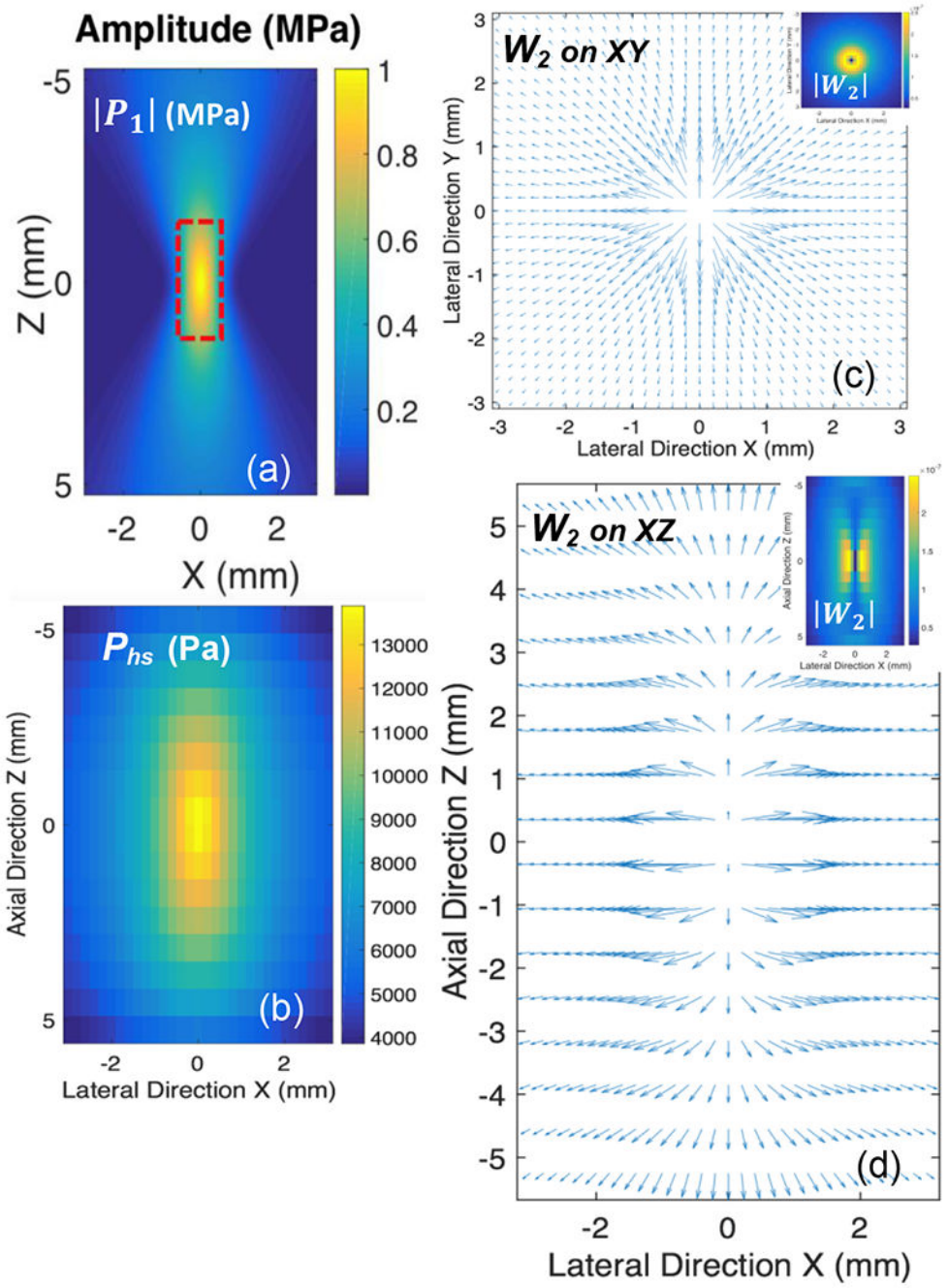

Fig.2:

(a) The amplitude of ultrasound pressure $|P_1|$ on XZ(Y = 0) plane. (b) Ultrasound-induced hydrostatic pressure P_{hs} on XZ(Y = 0) plane. (c)-(d) The exudation flow velocity (W_2) *on* XY(Z = 0) plane and XZ(Y = 0) plane, respectively. The inset of (c) and (d) is the amplitude distribution of W_2.

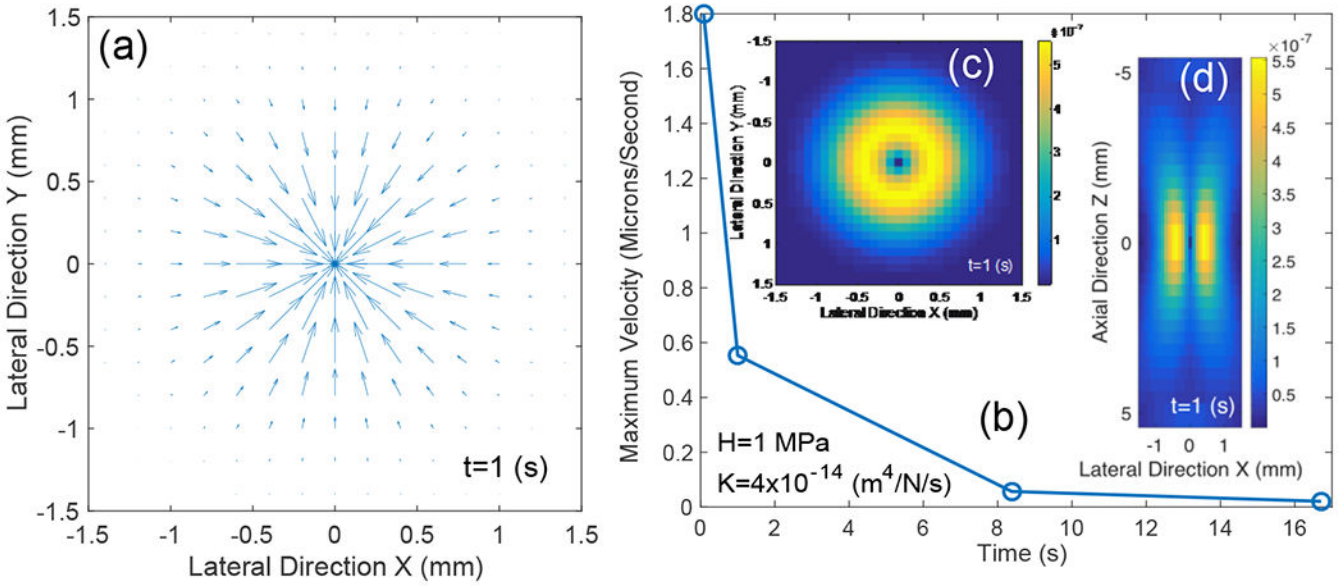

Fig.3:

(a) Backflow velocity (W_2) on XY(Z = 0) plane after ultrasound is off for 1 second. (b) The maximum backflow speed (W_2) as a function of time. (c-d) Amplitude distribution of the backflow W_2 on the XY(Z = 0) and XZ(Y = 0) planes, respectively.

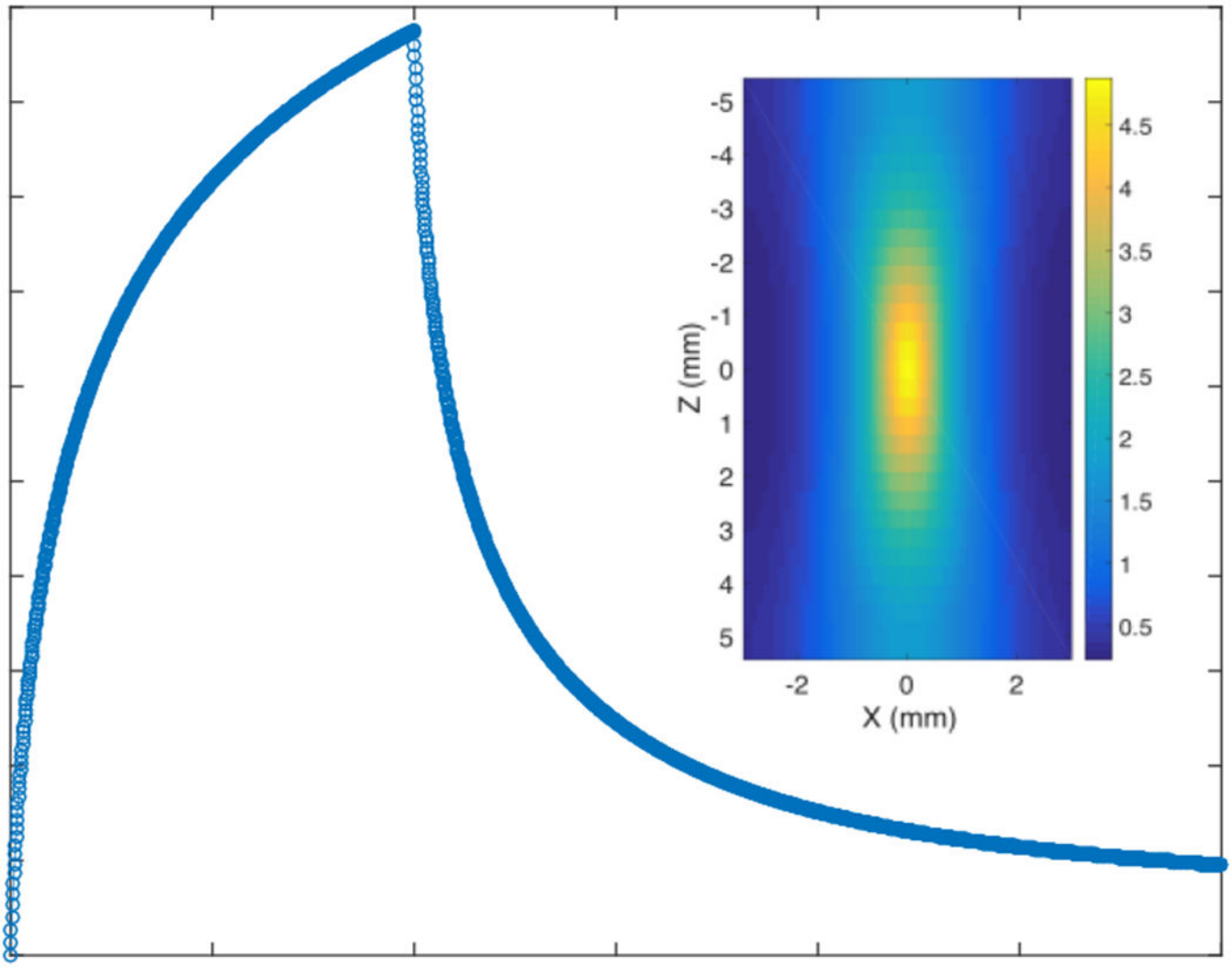

Fig.4:

Ultrasound-induced temperature change (ΔT) as a function of time at the center of the ultrasound focus. Ultrasound exposure time t_0 = 10 seconds. The inset is the 2D distribution of ΔT on the XZ(Y = 0) plane when t = t_0 = 10 seconds.

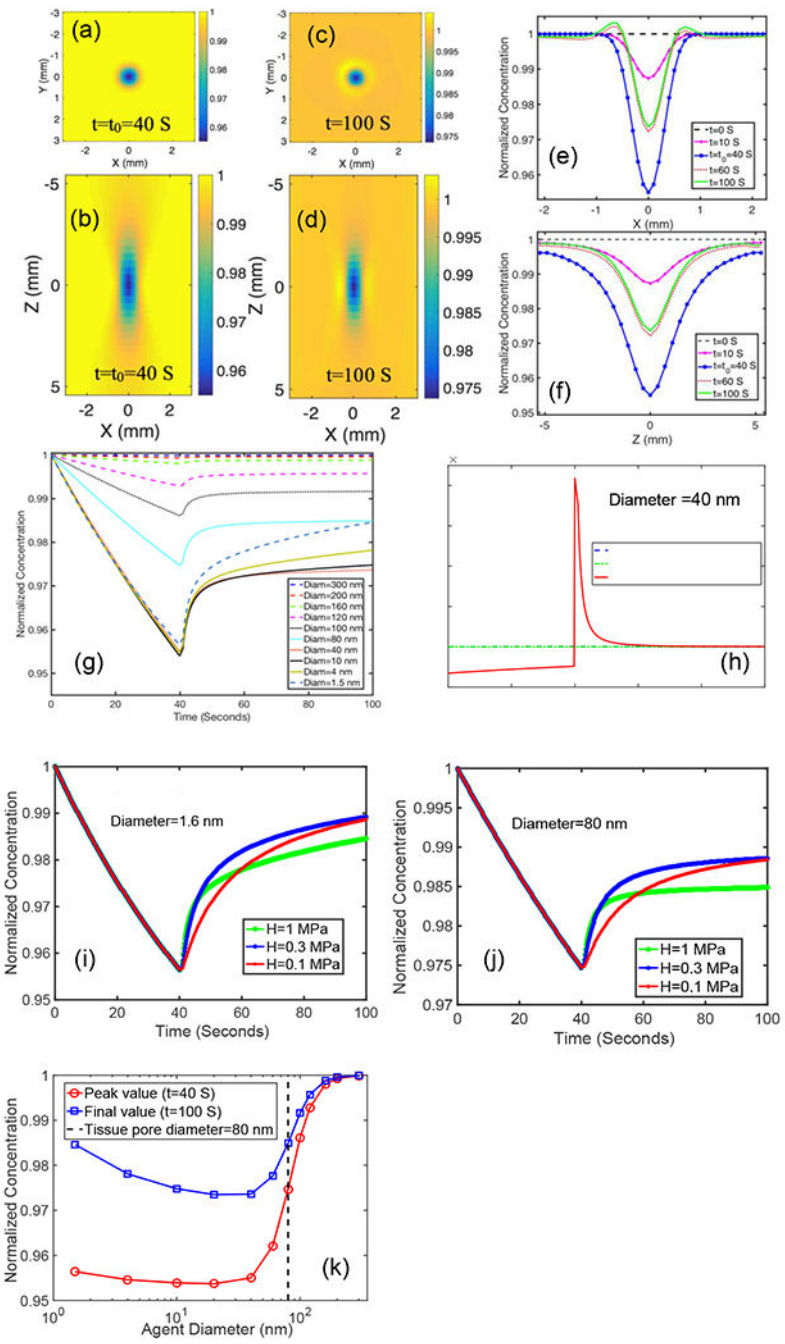

Fig.5:

The 2D distribution of the normalized concentration (C/C_0) of temperature-insensitive agents on the plane of (a) XY(Z = 0) and (b) XZ(Y = 0) at t = t_0 = 40 seconds (right after ultrasound is off); (c) XY(Z = 0) and (d) XZ(Y = 0) at t = 100 seconds; (e) 1D distribution of the normalized concentration along (e) X and (f) Z direction at different times (note the agent in (a-f) has an average diameter of 40 nm); (g) the normalized concentration as a function of time at the center of the focus with different agent diameters; (h) the rates of the normalized concentration changes contributed from different mechanisms: diffusion-,

thermophoresis-, and ultrasound-induced fluid with an agent diameter of 40 nm; (i) the normalized concentration as a function of time at the center of the focus with different apparent moduli of H with an agent diameter of 1.6 nm; (j) the same as (i) with an agent diameter of 80 nm; (k) as a function of the agent diameter when $t=t_0=40$ and 100 seconds.

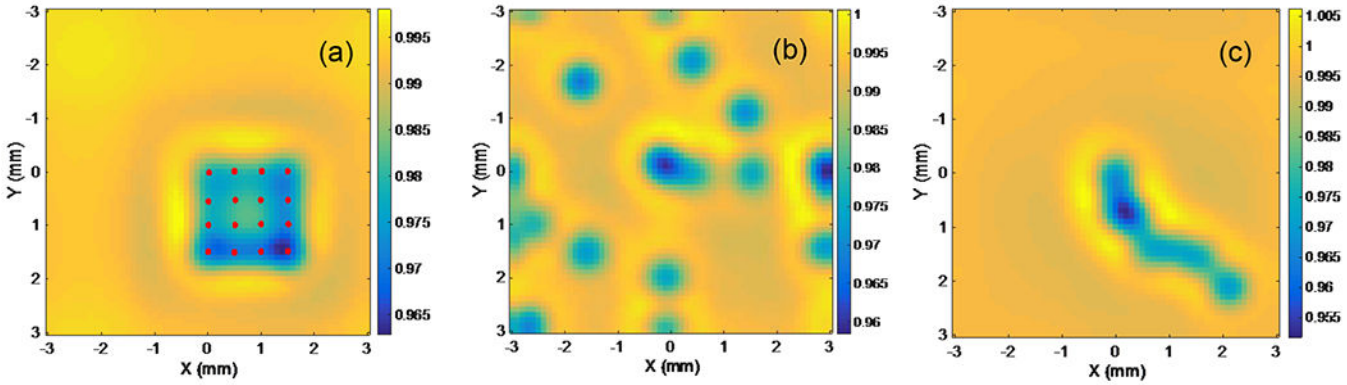

Fig.6:

Examples of the 2D distribution of the normalized concentration of agents on the XY(Z = 0) planes with multiple foci: (a) a total of 16 foci distributed on a 1.5x1.5 mm^2 square area and the red dots indicate each position of the focus; (b) a random distribution on the plane; (c) a random distribution along a curve.

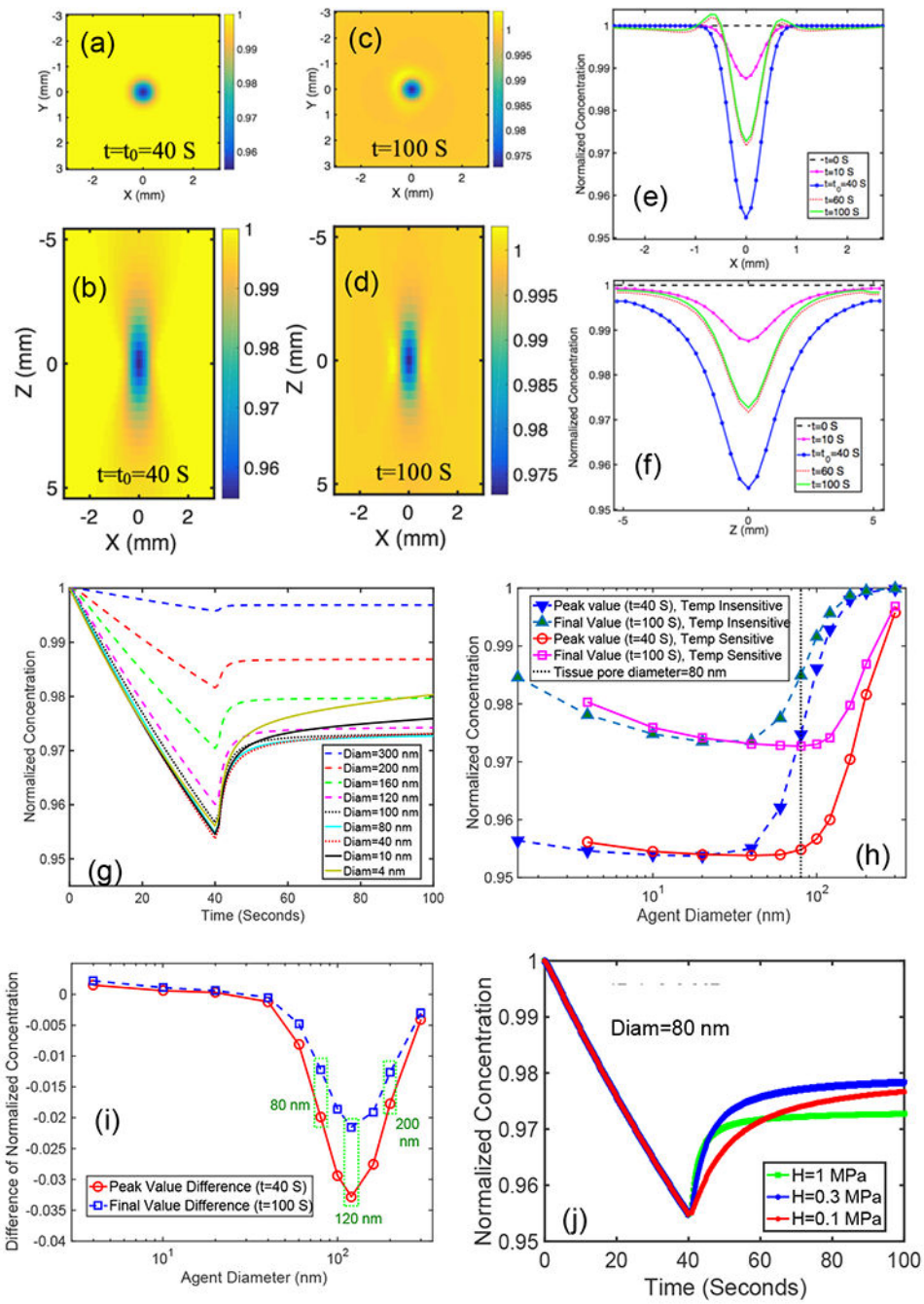

Fig.7:

Similar to Fig.5 but for temperature-sensitive agents. The 2D distribution of the normalized concentration (C/C_0) of the temperature-sensitive agents on the plane of (a) XY(Z = 0) and (b) XZ(Y = 0) at t = t_0 = 40 seconds (right after ultrasound is off); (c) XY(Z = 0) and (d) XZ(Y = 0) at t = 100 seconds; (e) 1D distribution of the normalized concentration along (e) X and (f) Z direction at different times (note that the agent in (a-f) has an average diameter of 80 nm); (g) the normalized concentration as a function of time at the center of the focus with different agent diameters; (h) a function of the agent diameter when t=t_0=40 and 100

seconds (note that the data shown in Fig.5(k) are also copied here for comparison between the two types of agents); (i) the difference of the normalized concentrations between the two types of agents as a function of agent diameter at $t = t_0 = 40$ and 100 seconds; (j) the normalized concentration as a function of time at the center of the focus with different apparent moduli of H with an agent diameter of 80 nm.

Table 1:

All equations. US: ultrasound

Eq #	Equation	US Status
0a	$P(r,t) = P_0(r) + P_1(r)\exp(-i\omega t) + P_2(r)\exp(-i2\omega t) + c.c.$	On
0b	$\rho(r,t) = \rho_0(r) + \rho_1(r)\exp(-i\omega t) + \rho_2(r)\exp(-i2\omega t) + c.c.$	On
0c	$V(r,t) = V_1(r)\exp(-i\omega t) + V_2(r)\exp(-i2\omega t) + c.c.$	On
1	$\nabla^2 P_{hs} \approx \frac{(\phi_f/\phi_s)}{\rho_0 K}\nabla \bullet \langle \rho_1 V_1 \rangle \approx -\frac{\alpha(\phi_f/\phi_s)}{c_0 K\omega^2 {\rho_0}^2}\left[\nabla P_1 \bullet \nabla P_1^*\right]$	On
2a	$W_2 = -K\nabla P_{hs};\ W_2 = -V_s;\ u_s = \int_0^{t0} V_s dt$	On
2b	$KH\nabla^2 u_s = \frac{\partial u_s}{\partial t} = V_s;\ W_2 = -V_s$	Off
3a	$\rho_0 c_t \frac{\partial(\Delta T)}{\partial t} = k_t \nabla^2(\Delta T) - \omega_b \rho_b c_b(\Delta T) + \frac{\alpha\lvert P_1\rvert^2}{\rho_0 c_0}$	On
3b	$\rho_0 c_t \frac{\partial(\Delta T)}{\partial t} = k_t \nabla^2(\Delta T) - \omega_b \rho_b c_b(\Delta T)$	Off
4	$\frac{\partial C}{\partial t} + \nabla \bullet J = \sigma_s - \sigma_i;\ J = -D_{BD}\nabla C - CD_{TP}\nabla(\Delta T) + CR_f W_2$	On & Off
5	$P_1(x,y,z) = \frac{P_a z_d}{2\sinh^2(kz_d)}\left[e^{kz_d}\frac{\sin(k\sqrt{D_-})}{\sqrt{D_-}} - e^{-kz_d}\frac{\sin(k\sqrt{D_+})}{\sqrt{D_+}}\right]$	On

Table 2:

Major variables, operators, physical meanings and adopted values in simulations that are modified based on following references.

ϕ_f and ϕ_s: (Raghavan, 2018); K: (Liu and Schlesinger, 2015); ω_b: (Curra et al., 2000); others:(Soneson, 2009) and the related manual of HIFU Simulator.

Quantity & Operator	Physical Meaning	Typical value (unit)
∇^2	Laplace operator	N/A
P_{hs}	Ultrasound-induced increase of the hydrostatic pressure of the interstitial fluid in tissue (it is the 2nd-order small quantity)	Dependent variable (Pa)
ϕ_f	Volume fraction of interstitial fluid in tissue	0.2 (no unit)
ϕ_s	Volume fraction of solid matrix in tissue ($= 1 - \phi_f$)	0.8 (no unit)
ρ_0, ρ_b	Average tissue density (it is the 0-order component of the density) Average blood density (it is the 0-order component of the density)	1,064 (Kg/m^3) 1,060 (Kg/m^3)
K	Tissue (or tumor) hydraulic conductivity (related to tissue permeability and fluid viscosity)	4x10^{-14} (m^4/N/s) (Tumor)
$\nabla \bullet$	Divergence operator	N/A
$\langle \rho_1 V_1 \rangle$	ρ_1 and V_1 are respectively the 1st-order oscillation of tissue density and velocity (caused by the ultrasound 1st-order pressure oscillation). $\langle \rho_1 V_1 \rangle$ is the time average in one oscillation cycle of the momentum in unit volume ($\rho_1 V_1$) caused by ultrasound.	Dependent variables ρ_1: Kg/m^3 V_1: m/s
α	Tissue ultrasound absorption coefficient. It is a function of angular frequency and its unit should be 1/m in equations 1 and 3a after considering the frequency effect. If the frequency is 1 MHz, its value is shown on the right.	0.58 (db/cm) or 0.58/8.686 (Np/cm)
c_0	Sound speed in tissue	1540 (m/s)
ω	Angular frequency of the adopted ultrasound	$2\pi \times 2.5$ MHz
∇P_1	P_1 is the 1st-order complex amplitude of the ultrasound pressure and ∇P_1 is the gradient of P_1 (it is a vector)	Dependent variables (Pa/m)
∇P_1^*	∇P_1^* is the complex conjugate of ∇P_1 (it is a vector)	Dependent variables (Pa/m)
$\bullet$	Vector dot product	N/A
c_t, c_b	Specific heat capacity of tissue and blood, respectively	4200, 3780 (J/kg/K)
k_t	Tissue thermal conductivity	0.6 (W/m/K)
ω_b	Blood perfusion rate	0.189 (1/s)